Mapping math xmlns="http://www.w3.org/1998/Math/MathML" display="inline">mrow>msub>mrow>mi>LiNbO/mi>/mrow>mrow>mn>3/mn>/mrow>/msub>/mrow>/math> Phonon-Polariton Nonlinearities with 2D THz-THz-Raman Spectroscopy

Haw-Wei Lin, Griffin Mead, and Geoffrey A. Blake

Mapping LiNbO$_3$ phonon-pariton nonlinearities with 2D THz-THz-Raman spectroscopy

Haw-Wei Lin,[*] Griffin Mead,[†] and Geoffrey A. Blake[‡]
(Dated: October 11, 2022)

Two-dimensional terahertz-terahertz-Raman spectroscopy (2D-TTR) can provide insight into the anharmonicities of low-energy phonon modes—knowledge of which can help develop coherent control strategies of material properties. Measurements on LiNbO$_3$ reveal THz and Raman nonlinear transitions between the E(TO$_1$) and E(TO$_3$) phonon-paritons. Distinct coherence pathways are observed with different THz polarizations. The observed pathways suggest that the origin of the third-order nonlinear responses is due to mechanical anharmonicities, as opposed to electronic anharmonicities. Further, we confirm that the E(TO$_1$) and E(TO$_3$) phonon-paritons are excited through resonant one-photon THz excitation.

Coherent control of lattice dynamics using ultrafast optical techniques can alter macroscopic properties of materials. Notable demonstrations include driving reversals of ferroelectric polarization [1], initiating magnetic phase transitions [2], and enhancing superconductivity [3]. However, optical fields can also produce parasitic electronic excitations within materials [4] and are fundamentally limited from phase-sensitive access to THz-energy phonon modes that are coupled to bulk material properties [5–9].

Recent developments of intense ultrafast terahertz (THz) sources present an exciting, if under-explored, alternative to optical fields for coherent control experiments [4, 7, 10]. With THz fields, it becomes possible to resonantly drive specific phonon modes with phase sensitivity and with no parasitic excitations. Unlike optical pulses, THz fields also offer an extra dimension of control since phonon excitations can proceed through both dipole- and polarizability-mediated transitions. Additionally, the fast-paced development of pulse shaping technologies [11–13] may present opportunities for creating tailored THz pulses which precisely manipulate specific material properties using knowledge of mechanical and electronic anharmonicities.

To reach this future degree of control over material properties, it is essential to be able to observe and interpret the multitude of different linear and nonlinear excitation pathways that occur within a material when pumped with an intense, broadband THz field. These kinds of "mapping" experiments reveal information on a material's potential energy landscape, excitation pathways, and dominant anharmonicities, thus laying the foundation for future mode-selective coherent control experiments and applications.

Lithium niobate (LiNbO$_3$) is a fundamental material in nonlinear optics due to its large ferroelectric response and nonlinear susceptibility [14, 15]. Phonon-paritons (PhP) in LiNbO$_3$ have been linked to orders of magnitude enhancements of the second-order susceptibility in the low THz frequency regime [5]. LiNbO$_3$ is also notably used for generating intense THz pulses using velocity-matched tilted-pulse-fronts [16–19, 39]. The unique prop-
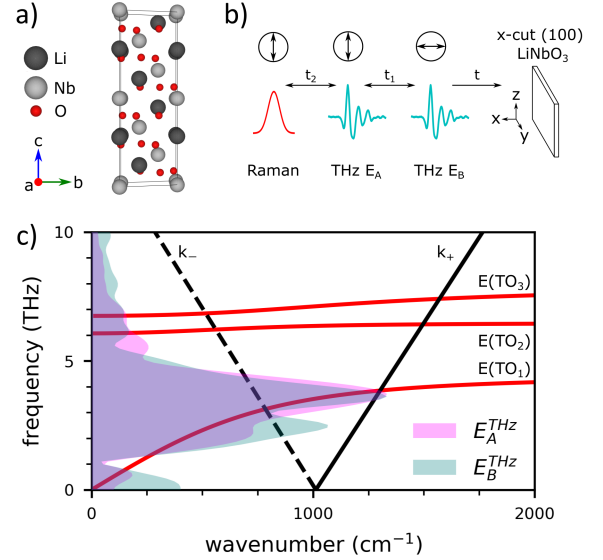

FIG. 1. a) LiNbO$_3$ crystal structure in the hexagonal unit cell [21, 22]. b) Schematic of the 2D-TTR experiment, pulse sequence, and time definitions. The polarization of each pulse is indicated in the circles. Coordinates $\{x, y, z\}$ refer to the crystal axes of x-cut LiNbO$_3$, where x and z coincide with unit cell vectors a and c, and y is orthogonal to x and z. c) Red: PhP dispersion curve for E-symmetry phonon modes [23]. Black: wavevector matching condition of the 800 nm probe for forward (k_+, solid) and backward (k_-, dashed) propagating PhPs [19]. The shaded regions show the THz bandwidth of E_A^{THz} and E_B^{THz}.

erties and numerous applications of LiNbO$_3$ suggest it as an ideal model candidate for developing techniques which can map out phonon mode anharmonicities.

In this letter, we demonstrate the use of two-dimensional terahertz-terahertz-Raman (2D-TTR) spectroscopy to characterize the potential energy surface (PES) of E-symmetry phonon modes in x-cut congruent LiNbO$_3$. The excitation mechanism, nonlinear phonon-phonon couplings, and the primary source of anharmonicity for the E-symmetry phonon modes are directly determined from the third-order nonlinear response.

2D-TTR spectroscopy. — While time intensive, multi-dimensional spectroscopy is a powerful tool for disentangling overlapping spectral features, determining the timescales of the underlying processes, and revealing couplings between spectral modes [24–27]. Hybrid THz-Raman third-order spectroscopies have been suggested as ideal tools for characterizing solid state PESs [6, 24]. We employ 2D-TTR spectroscopy, a multidimensional extension of THz Kerr effect (TKE) spectroscopy in which an additional time delay t_1 is introduced between two THz pump pulses [25, 28], to study $LiNbO_3$.

The third-order nonlinear polarization induced by the 2D-TTR pulse sequence (Fig. 1b) is given as

$$P^{(3)}(t) = E_{probe}(t) \iint dt_1 dt_2 R^{(3)}(t_1, t_2) \\ E_A^{THz}(t - t_2) E_B^{THz}(t - t_1 - t_2) \quad (1)$$

The third-order response function $R^{(3)}(t_1, t_2)$ contains both resonant one-photon absorption (1PA)

$$tr\langle\alpha(t_1 + t_2)[\mu(t_1), [\mu(0), \rho]]\rangle$$

and sum-frequency two-photon absorption (2PA)

$$tr\langle\alpha(t_1 + t_2)[\alpha(0), \rho]\rangle$$

THz excitation pathways, where μ and α are the transition dipole and polarizability operators, respectively, and ρ is the equilibrium density matrix [25]. Both E- and A_1-symmetry phonons in $LiNbO_3$ ($R3c$ space group) are Raman- and IR-active and can be simultaneously excited with broadband THz pulses. However, the cross-polarized Raman probe setup is selectively sensitive to E-symmetry phonons (see SI for details). The wavevector matching condition for the E-symmetry PhPs and the available THz pump bandwidths are shown in Fig. 1c, highlighting the broadband pump pulses used have sufficient bandwidth to induce either 1PA or 2PA excitations up to the $E(TO_3)$ mode.

While the optical excitation mechanism of PhPs in $LiNbO_3$ is quite well-understood [16, 19, 29], the excitation mechanism of PhPs with THz frequency pulses remains unclear. The forward-propagating $E(TO_1)$ PhP has been studied with TKE spectroscopy [17] and 2D-TTR spectroscopy with two parallel-polarization THz pulses [6]. In this 2D-TTR setup, the single-pump, lower-order signals are also recorded, which are significantly more intense than the double-pump signals that strongly depend on excitation mechanism, phonon-phonon couplings, and anharmonicity. While these data are well-suited for coupled-equations of motion models for the phonon modes, the nonlinear signatures of interest can be obstructed in 2D frequency space and may require significant THz field strengths to be observable. This is the case in $LiNbO_3$, where 2D spectra modelling do not conclusively determine whether the excitation of the

$E(TO_1)$ PhP proceeds through a 2PA or anharmonic 1PA mechanism [6]. Higher frequency PhPs that are observed with optical Raman excitations [19] also remained unexplored with THz excitations due to the limited THz bandwidth available in previous TKE and 2D-TTR experimental studies of $LiNbO_3$.

In contrast to earlier 2D-TTR experiments on $LiNbO_3$ [6, 24], we utilized orthogonal THz pump pulses and careful differential chopping to rigorously remove single-pump and second-order contributions, which are difficult to remove in 1D-TKE spectroscopy and do not provide definitive information on excitation mechanism and anharmonic phonon-phonon couplings. This is crucial for studying phonon modes that are both Raman- and IR-active, where the large number of possible 1D excitation pathways can easily overwhelm weaker nonlinear features of the PES and overcrowd the 2D spectra. Two separate THz emitters are used for THz generation to prevent emitter dynamics from contaminating the 2D-TTR spectra. Further, by varying the crystal orientation and the time ordering of the THz pump pulses, four independent elements of $R^{(3)}$ are measured with 2D-TTR.

$LiNbO_3$ has also been studied by 2D-THz spectroscopy, the direct analog of 2D-IR in the THz frequency range [30]. The emitted signal in 2D-THz are attributed to THz field-induced interband-tunnelling of electrons into the conduction band. Due to the moderate THz frequency (< 2 THz) used in the 2D-THz experiment, near DC nonlinear effects are dominant and anharmonic phonon dynamics remain unexplored. Our experiments employ higher field strength (> 1 MV/cm) and bandwidth, which enables exploration of PhP modes up to ~ 9 THz to characterize the excitation pathways and nonlinearities.

Resonant excitation of $E(TO_1)$ and $E(TO_3)$. — The time domain 2D-TTR spectra of 0.5 mm thick x-cut $LiNbO_3$ measured at $E_{probe} \parallel z$ and $E_{probe} \parallel y$ are provided in the SI. Note that the coordinates $\{x, y, z\}$ refer to the crystal axes of x-cut $LiNbO_3$ throughout this letter. The response exhibits an oscillatory behavior along t_1 and a damped exponential along t_2 with oscillatory features near $t_2 = 0$. A prolonged t_1 response extending far outside the THz field-overlap region (roughly $-0.5 \le t_1 \le 0.5$ ps) provides clear evidence of long-lived dynamics after the first THz pulse, indicating that the 1PA contribution to $R^{(3)}$ is dominant compared to that from 2PA pathways. The 2PA contribution to 2D-TTR only exists in the THz field overlap region near $t_1 = 0$ (see SI for details); whereas, the extent of the 1PA pathway is determined by the dephasing time of the coherent state, which typically extends several picoseconds outside the field overlap region.

The different nonlinear contributions to the time domain signal can be separated in 2D frequency space through a 2D fast Fourier transform (2D-FFT). To extract the nuclear components of $R^{(3)}$, the region $-0.75 \le$
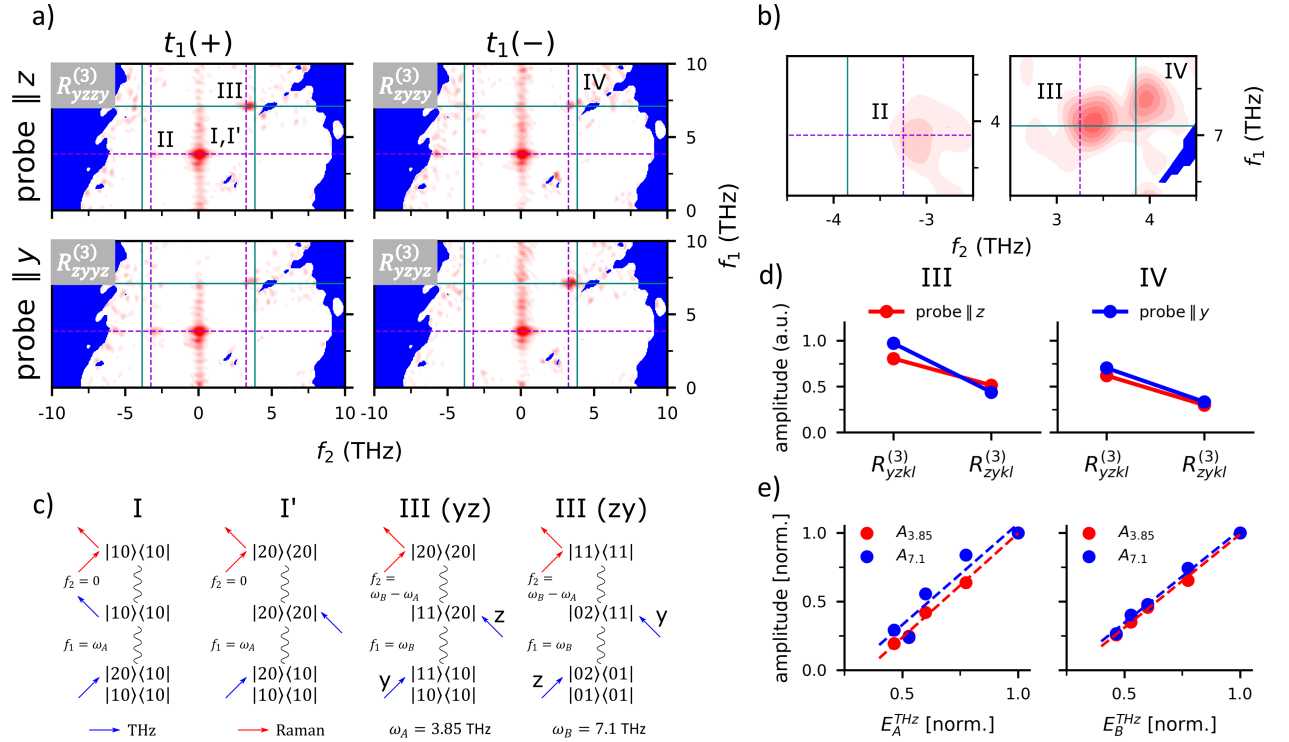
FIG. 2. a) 2D-TTR spectra in the frequency domain for four pump-probe polarization configurations, taken from the combination of two crystal orientations and two THz polarization orderings (positive and negative t_1 quadrants). The spectra have been deconvolved by the IRF to reveal true intensity and frequency positions. Guiding lines are provided at $f_1 = 3.85$ THz (violet), $f_1 = 7.1$ THz (teal), $f_2 = \pm 3.25$ THz (violet) and $f_2 = \pm 3.85$ THz (teal). b) Zoom-in of peaks II to IV for polarization $R_{zyzy}^{(3)}$. c) Select Feynman pathways for the observed nonlinear peaks (I, I') and III. Depending on the THz polarizations, III (yz) or III (zy) is selectively observed. See SI for full assignment. d) THz polarization dependence of the FT amplitude of peaks III and IV. e) THz field strength dependence of the $E(TO_1)$ ($A_{3.85}$) and $E(TO_3)$ ($A_{7.1}$) features along f_1. Best linear fits are shown as dashed lines.

$t_1 \leq 0.75$ ps is removed prior to 2D-FFT to avoid coherent artifacts present in the field-overlap region. After 2D-FFT, the spectra is deconvolved by the instrument response function (IRF) [25, 31]. As described in equation (1), the measured spectra are a convolution of $R^{(3)}$ with the structured THz pulses in the time domain. The IRF is experimentally measured using the third-order electronic response of 100 μm GaP [25]. Applying the convolution theorem, the deconvolution process becomes a simple division of the 2D-FFT spectra of LiNbO$_3$ by the IRF spectra in the frequency domain. The deconvolved 2D-FFT results for all four polarization configurations are shown in Fig. 2a. The regions of low deconvolution confidence (less than 5% IRF amplitude) are marked with solid blue. Tensor notation $R_{ijkl}^{(3)}$ is used to denote the pump-probe polarizations, in which $ijkl$ corresponds to the polarization of the first and second THz pulse, the probe pulse, and the detected third-order polarization respectively.

Four main 2D spectral features, labelled I to IV, are observed. The pairs of spectra with identical THz polarization ($R_{yzzy}^{(3)}$ and $R_{yzyz}^{(3)}$; $R_{zyzy}^{(3)}$ and $R_{zyyz}^{(3)}$) show strong similarities in peak positions and intensity. This is due to selection rules for y and z polarized THz pulses and will be discussed in detail below. A dominant peak (I,I') at $(f_1, f_2) = (3.85, 0)$ THz is apparent in the spectra, corresponding to the main features along t_1 (E(TO$_1$) damped harmonic oscillation) and t_2 (exponential decay). Two weaker peaks (II and III) are observed at $(f_1, f_2) = (3.85, \sim -3.25)$ and ($\sim 7.1, \sim 3.25$). An additional peak (IV) can be observed near peak III at ($\sim 7.1, \sim 3.85$) for $R_{zyzy}^{(3)}$ and $R_{zyyz}^{(3)}$.

The ~ 7.1 THz features correspond to the E(TO$_3$) PhP. Energy conservation and momentum considerations suggest that the forward-propagating PhP is excited by the THz pump pulses. This feature has not been observed in previous TKE studies of LiNbO$_3$ [6, 17] likely due to THz bandwidth limitations (< 5 THz). While the E(TO$_2$) phonon is within the THz bandwidth, due to the order-of-magnitude lower transition dipole strength compared to E(TO$_1$) and E(TO$_3$) [23], no associated dynamics are observed. With $f_1 = 7.1$ assigned to E(TO$_3$) PhP, it is natural to assign $f_2 = \pm 3.25$ to the difference frequency of E(TO$_1$) and E(TO$_3$) PhPs. The field strength
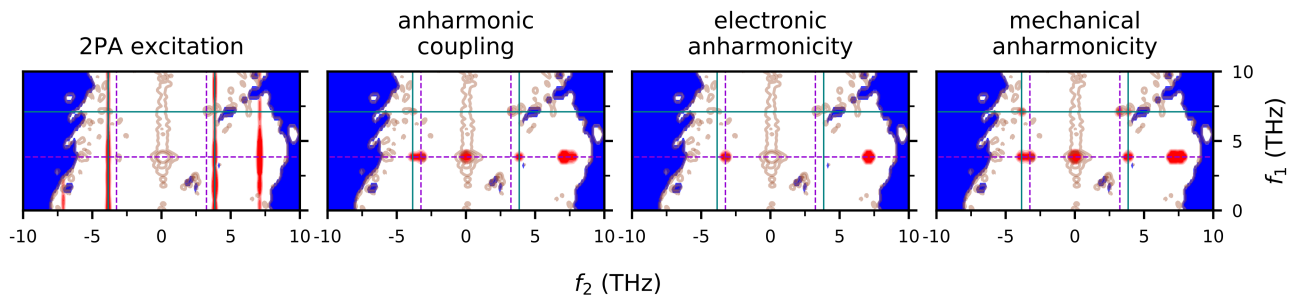
FIG. 3. Third-order models based on different excitation mechanisms and sources of anharmonicity. Identical guiding lines are added. For reference, the overlayed contours depict the $R_{zyzy}^{(3)}$ experimental spectra.

dependence of the $f_1 = 3.85$ THz and $f_1 = 7.1$ THz features are measured (Fig. 2e), and both peaks show linear dependence with respect to the field strength of THz pump A and B, i.e., $S_{3.85}, S_{7.1} \propto E_A^{THz} \cdot E_B^{THz}$, confirming that the observed signals are third-order in nature. Thus, the linear power scaling and the extended dynamics along t_1 provide direct evidence that both E(TO$_1$) and E(TO$_3$) PhPs originate from resonant 1PA THz excitations.

Polarization dependence of nonlinear transitions.— To analyze the intensity changes observed with different THz polarizations, we perform a Feynman pathway analysis to examine the quantum state of the system after each field interaction. Unlike 2D-IR spectroscopy, whose pathways only involve one-quanta transitions, 2D-TTR pathways must include a nonlinear transition due to its three-pulse sequence. The lowest-order pathways consist of two one-quanta transitions and one zero- or two-quanta transition [26]. Consequently, the peak positions can not only arise at resonant frequencies of the vibrational modes, but also at zero, second-harmonic, sum- and difference-frequencies. Feynman pathway assignments for peaks I and III are provided in Fig. 2c (full assignment in SI). The double-sided Feynman diagram notation $|n_1 n_3\rangle \langle n_1 n_3|$ is used to denote the density matrix of the system, where n_1 and n_3 are the number of quanta in E(TO$_1$) and E(TO$_3$) respectively. Field-induced excitation and de-excitation are represented by inward and outward arrows. Further, THz transitions are only allowed if the momentum of the THz photon maps onto the PhP dispersion curves. We confirmed that conservation of momentum is preserved in the Feynman pathways presented (see SI for details on momentum conservation in nonlinear transitions).

Pathway I involves two one-quanta THz transitions and a final zero-quanta Raman transition. Symmetry analysis shows that the $|00\rangle \rightarrow |10\rangle$ transition is symmetry-forbidden for $E^{THz} \parallel z$; whereas, the transition $|10\rangle \rightarrow |20\rangle$ is symmetry-allowed for both $E^{THz} \parallel z$ and $E^{THz} \parallel y$. Thus, the proposed Feynman pathway I starts from the $|10\rangle \langle 10|$ population state and is symmetry-allowed for both THz polarization ordering

$ij = yz$ and zy. The low energy of the phonon modes compared to thermal energy $k\mathrm{T} = 6.2$ THz at room temperature makes the excited population state available.

Next, we examine peaks II-IV, whose intensities are strongly dependent on THz polarization. For example, the FT amplitude is larger in THz polarization yz than zy for peaks III and IV (Fig. 2d). Due to selection rules for E-symmetry phonons, the two THz polarizations yz and zy result in distinct symmetry-allowed Feynman pathways (Fig. 2c for peak III). Notably, the starting state is different for the two polarizations. Considering only thermodynamic effects on the starting state population, the Boltzmann factor $e^{-(\omega_1 - \omega_2)/k\mathrm{T}}$ predicts for peaks III and IV a 1.7-fold and 1.9-fold increase in amplitude for polarization yz over zy, which is consistent with the experiment for both probe polarization. Follow-up measurements of low temperature LiNbO$_3$ 2D-TTR spectra would be highly informative for the Feynman pathway assignments.

Origin of anharmonicity.— A third-order 2D-TTR signal must involve a nonlinear transition in the resonant 1PA pathway. Consequently, 2D-TTR spectroscopy is highly sensitive to the anharmonicities present in the system, because the allowed nonlinear zero- or two-quanta transitions depend on the type of anharmonicity. We implement the anharmonic coupling model proposed by Sidler and coworkers [26], which considers resonant 1PA pathways induced via electronic and mechanical anharmonicities. Electronic anharmonicity refers to the nonlinear contributions to the transition dipole and polarizability operators of the vibrational mode [27]. For two normal modes E(TO$_1$) and E(TO$_3$) with coordinates $\hat{q}_{E_1}$ and $\hat{q}_{E_3}$, the lowest order nonlinear dipole operator can be written as

$$\hat{\mu} \approx \mu^{(0)} \hat{q}_{E_1} + \mu^{(1)} \hat{q}_{E_1} \hat{q}_{E_3}$$

Alternatively, mechanical anharmonicity refers to perturbations to the Hamiltonian of the system, which includes both PES anharmonicity of the individual modes ($\hat{H}_{E_1}^{(1)}$ and $\hat{H}_{E_3}^{(1)}$) as well as cross-coupling terms between modes ($\hat{H}_{E_1 E_3}^{(1)}$). Here, we considered an anharmonic

cross-coupling term of the form

$$\hat{H}_{AB}^{(1)} = \lambda_{AAB} \hat{q}_A^2 \hat{q}_B$$

with sum over all modes $A, B = \{E(TO_1), E(TO_3)\}$.

For completeness, a model that considers the 2PA excitation pathway is also implemented (details in SI). As a first approximation, we assign equal intensity to all possible transitions. After applying convolution with the experimental IRF, the results are shown in Fig. 3. Critically, these models are constructed to include only third-order signals that involve both pump electric fields to account for the experimental differential chopping of 2D-TTR spectroscopy. One major benefit of selectively measuring the third-order 2D-TTR signal is the distinctness between signals from 2PA and 1PA pathways. The 2PA excitation pathway produces characteristic "streaking" patterns along f_1 [25], while 1PA pathways produce peaks at unique frequency positions [26]. Consistent with the Feynman pathway analysis presented above, the 2D-TTR spectra resemble much more closely to the 1PA anharmonic coupling model. By examining the individual sources of anharmonicity, it is clear that peaks I, III, IV can only be induced by mechanical anharmonicity, while peak II can be induced by both mechanical and electronic anharmonicity. These models strongly suggest that the observed 2D features are primarily induced via mechanical anharmonicity. A few additional peaks predicted by the mechanical anharmonicity model are not observed experimentally possibly due to limited THz power at the frequencies required for the nonlinear transition. For instance, the peaks at $(3.85, \pm 3.85)$ involve nonlinear zero- or two-quanta THz transitions of the $E(TO_1)$ mode, which require significant power at near DC or ~ 8 THz.

Conclusion.— We demonstrate that 2D-TTR spectroscopy can provide detailed information on the excitation mechanism, nonlinear phonon-phonon couplings, and sources of anharmonicity in phonon-polariton (PhP) dynamics of x-cut $LiNbO_3$. The wider bandwidths employed in this study allow investigation of both $E(TO_1)$ and $E(TO_3)$ PhPs. The selective measurement of the third-order response removes the single-pump contributions that dominate the 1D-TKE response and focuses on 2D signatures that are highly sensitive to the anharmonicity of the potential energy landscape. Feynman pathway analysis reveals THz and Raman nonlinear transitions between the $E(TO_1)$ and $E(TO_3)$ PhPs. We further determined that the $E(TO_1)$ and $E(TO_3)$ phonon-polaritons are excited through resonant 1PA THz excitations. Distinct Feynman coherent pathways are observed for different THz polarizations due to THz selection rules. 2PA excitation and 1PA anharmonic coupling models are constructed for third-order double-pumped pathways. The measured 2D-TTR spectra is most consistent with 1PA anharmonic coupling model induced via mechanical anharmonicity as opposed to electronic anharmonicity.

These findings provide an important foundation for future coherent control applications. A key demonstration of coherent control of vibrational states is the selective transfer of population [32–34]. The $|01\rangle \rightarrow |10\rangle$ nonlinear transition revealed in this work could be exploited with two THz pulses with tailored phase and bandwidth to achieve efficient population transfer between $E(TO_1)$ and $E(TO_3)$.

* Division of Chemistry and Chemical Engineering, California Institute of Technology, Pasadena, California 91125, United States

† Division of Chemistry and Chemical Engineering, California Institute of Technology, Pasadena, California 91125, United States. Current institution: Communications Technology Laboratory, National Institute of Standards and Technology, Boulder, Colorado 80305, United States

‡ gab@caltech.edu; Division of Chemistry and Chemical Engineering and Division of Geology and Planetary Sciences, California Institute of Technology, Pasadena, California 91125, United States

[1] R. Mankowsky, A. V. Hoegen, M. Frst, and A. Cavalleri, Ultrafast reversal of the ferroelectric polarization, Physical Review Letters **118**, 197601 (2017).

[2] D. Afanasiev, J. R. Hortensius, B. A. Ivanov, A. Sasani, E. Bousquet, Y. M. Blanter, R. V. Mikhaylovskiy, A. V. Kimel, and A. D. Caviglia, Ultrafast control of magnetic interactions via light-driven phonons, Nature Materials **20**, 607 (2021).

[3] R. Mankowsky, A. Subedi, M. Frst, S. O. Mariager, M. Chollet, H. T. Lemke, J. S. Robinson, J. M. Glownia, M. P. Minitti, A. Frano, M. Fechner, N. A. Spaldin, T. Loew, B. Keimer, A. Georges, and A. Cavalleri, Nonlinear lattice dynamics as a basis for enhanced superconductivity in $YBa_2Cu_3O_{6.5}$, Nature **516**, 71 (2014).

[4] S. Maehrlein, A. Paarmann, M. Wolf, and T. Kampfrath, Terahertz sum-frequency excitation of a Raman-active phonon, Physical Review Letters **119**, 127402 (2017).

[5] Y. Lu, Q. Zhang, Q. Wu, Z. Chen, X. Liu, and J. Xu, Giant enhancement of THz-frequency optical nonlinearity by phonon polariton in ionic crystals, Nature Communications **12**, 1 (2021).

[6] B. E. Knighton, R. T. Hardy, C. L. Johnson, L. M. Rawlings, J. T. Woolley, C. Calderon, A. Urrea, and J. A. Johnson, Terahertz waveform considerations for nonlinearly driving lattice vibrations, Journal of Applied Physics **125**, 10.1063/1.5052638 (2019).

[7] A. A. Melnikov, K. N. Boldyrev, Y. G. Selivanov, V. P. Martovitskii, S. V. Chekalin, and E. A. Ryabov, Coherent phonons in a Bi_2Se_3 film generated by an intense single-cycle THz pulse, Physical Review B **97**, 214304 (2018).

[8] M. J. Neugebauer, D. M. Juraschek, M. Savoini, P. Engeler, L. Boie, E. Abreu, N. A. Spaldin, and S. L. Johnson, Comparison of coherent phonon generation by electronic and ionic Raman scattering in LaAlO₃, Physical Review Research **3**, 013126 (2021).

[9] D. M. Juraschek, D. S. Wang, and P. Narang, Sum-frequency excitation of coherent magnons, Physical Review B **103**, 10.1103/PhysRevB.103.094407, 094407 (2021).

[10] D. M. Juraschek and S. F. Maehrlein, Sum-frequency ionic Raman scattering, Physical Review B **97**, 174302 (2018).

[11] V. Juv, G. Vaudel, Z. Ollmann, J. Hebling, V. Temnov, V. Gusev, and T. Pezeril, Ultrafast tunable modulation of light polarization at terahertz frequencies, Optics Letters **43**, 5905 (2018).

[12] C. Vicario, A. Trisorio, S. Allenspach, C. Regg, and F. Giorgianni, Narrow-band and tunable intense terahertz pulses for mode-selective coherent phonon excitation, Applied Physics Letters **117**, 1 (2020).

[13] B. Liu, H. Bromberger, A. Cartella, T. Gebert, M. Frst, and A. Cavalleri, Generation of narrowband, high-intensity, carrierenvelope phase-stable pulses tunable between 4 and 18 THz, Conference on Lasers and Electro-Optics, CLEO 2017 - Proceedings , 1 (2017).

[14] S. Sanna, S. Neufeld, M. Rsing, G. Berth, A. Zrenner, and W. G. Schmidt, Raman scattering efficiency in LiTaO₃ and LiNbO₃ crystals, Physical Review B - Condensed Matter and Materials Physics **91**, 224302 (2015).

[15] S. Sanna and W. G. Schmidt, Lithium niobate x-cut, y-cut, and z-cut surfaces from ab initio theory, Physical Review B - Condensed Matter and Materials Physics **81**, 214116 (2010).

[16] Y. Ikegaya, H. Sakaibara, Y. Minami, I. Katayama, and J. Takeda, Real-time observation of phonon-polariton dynamics in ferroelectric LiNbO₃ in time-frequency space, Applied Physics Letters **107**, 10.1063/1.4928480 (2015).

[17] B. S. Dastrup, J. R. Hall, and J. A. Johnson, Experimental determination of the interatomic potential in LiNbO₃ via ultrafast lattice control, Applied Physics Letters **110**, 10.1063/1.4980112 (2017).

[18] B. E. Knighton, B. S. Dastrup, C. L. Johnson, and J. A. Johnson, Measurement of a phonon-polariton dispersion curve by varying the excitation wavelength, Physical Review B **97**, 214307 (2018).

[19] T. Kuribayashi, T. Motoyama, Y. Arashida, I. Katayama, and J. Takeda, Anharmonic phonon-polariton dynamics in ferroelectric LiNbO₃ studied with single-shot pump-probe imaging spectroscopy, Journal of Applied Physics **123**, 10.1063/1.5021379 (2018).

[39] S. Kojima, Broadband terahertz spectroscopy of phonon-polariton dispersion in ferroelectrics, Photonics **5**, 1 (2018).

[21] V. Caciuc, A.V. Postnikov, and G. Borstel, Ab initio structure and zone-center phonons, Physical Review B - Condensed Matter and Materials Physics **61**, 8806 (2000).

[22] K. Momma and F. Izumi, Vesta 3 for three-dimensional visualization of crystal, volumetric and morphology data, Journal of Applied Crystallography **44**, 1272 (2011).

[23] A. S. Barker and R. Loudon, Dielectric properties and optical phonons in LiNbO₃, Physical Review **158**, 433 (1967).

[24] C. L. Johnson, B. E. Knighton, and J. A. Johnson, Distinguishing nonlinear terahertz excitation pathways with two-dimensional spectroscopy, Physical Review Letters **122**, 073901 (2019).

[25] G. Mead, H. W. Lin, I. B. Magdu, T. F. Miller, and G. A. Blake, Sum-frequency signals in 2D-terahertz-terahertz-Raman spectroscopy, Journal of Physical Chemistry B **124**, 8904 (2020).

[26] D. Sidler and P. Hamm, A Feynman diagram description of the 2D-Raman-THz response of amorphous ice, Journal of Chemical Physics **153**, 10.1063/5.0018485 (2020).

[27] D. Sidler and P. Hamm, Feynman diagram description of 2D-Raman-THz spectroscopy applied to water, Journal of Chemical Physics **150**, 10.1063/1.5079497 (2019).

[28] I. A. Finneran, R. Welsch, M. A. Allodi, T. F. Miller, and G. A. Blake, Coherent two-dimensional terahertz-terahertz-Raman spectroscopy, Proceedings of the National Academy of Sciences **113**, 6857 (2016).

[29] K. Matsumoto and T. Satoh, Selective imaging of the terahertz electric field of the phonon-polariton in LiNbO₃, Physical Review B **102**, 094313 (2020).

[30] C. Somma, K. Reimann, C. Flytzanis, T. Elsaesser, and M. Woerner, High-field terahertz bulk photovoltaic effect in lithium niobate, Physical Review Letters **112**, 10.1103/PhysRevLett.112.146602, 146602 (2014).

[31] G. Ciardi, A. Berger, P. Hamm, and A. Shalit, Signatures of intra- and intermolecular vibrational coupling in halogenated liquids revealed by two-dimensional Raman-terahertz spectroscopy, The Journal of Physical Chemistry Letters **10**, 4463 (2019).

[32] A. Owens, A. Yachmenev, and J. Kpper, Coherent control of the rotation axis of molecular superrotors, Journal of Physical Chemistry Letters **9**, 4206 (2018).

[33] T. G. Park, H. R. Na, S. H. Chun, W. B. Cho, S. Lee, and F. Rotermund, Coherent control of interlayer vibrations in Bi₂Se₃ van der waals thin-films, Nanoscale **13**, 19264 (2021).

[34] J. G. Horstmann, H. Bckmann, B. Wit, F. Kurtz, G. Storeck, and C. Ropers, Coherent control of a surface structural phase transition, Nature **583**, 232 (2020).

[35] See Supplemental Material for details on the experimental setup, modelling of the 2D-TTR signal, and complete Feynman analysis, which includes Refs. [36-41].

[36] I. B. Magdu, G. J. Mead, G. A. Blake, and T. F. Miller, Interpretation of the Thz-Thz-Raman spectrum of bromoform, Journal of Physical Chemistry A **123**, 7278 (2019).

[37] P. Hamm and M. Zanni, *Concepts and Methods of 2D Infrared Spectroscopy* (Cambridge University Press, 2011).

[38] S. Kojima, Terahertz polariton dispersion in uniaxial optical crystals, Progress in Electromagnetics Research Letters **77**, 109 (2018).

[39] S. Kojima, Broadband terahertz spectroscopy of phonon-polariton dispersion in ferroelectrics, Photonics **5**, 1 (2018).

[40] A. Cammarata, Phonon-phonon scattering selection rules and control: An application to nanofriction and thermal transport, RSC Advances **9**, 37491 (2019).

[41] R. Yang, S. Yue, Y. Quan, and B. Liao, Crystal symmetry based selection rules for anharmonic phonon-phonon scattering from a group theory formalism, Physical Review B **103**, 184302 (2021).